A Transonic Wing-Body Flowfield Calculation with Improved Grid Topology

L. T. Chen,* J. C. Vassberg,† and C. C. Peavey‡
Douglas Aircraft Company, Long Beach, California

A transonic wing-body flowfield computational method has been developed. The method uses an improved grid topology, introduces a hybrid mapping/numerical grid-generation scheme, and incorporates new artificial viscosities and shock-point operators into existing multigrid finite volume codes. The improved grid topology yields better fuselage geometry definition and a more nearly orthogonal mesh distribution than existing grid topologies. The hybrid mapping/numerical grid-generation scheme applies a conformal mapping procedure in the far field and a nearly orthogonal numerical scheme in the near field. The scheme is general, efficient, and generates nearly orthogonal grid systems in both the far and near fields. Both the use of the multigrid method in the flow solver and the improvement of mesh orthogonality in the grid generation reduce the number of iteration cycles required for a converged flow solution. Nonconservative and partially conservative artificial viscosities and shock-point operators incorporated into the flow solver improve the prediction of shocks.

Introduction

SIGNIFICANT progress has been made in developing transonic flow computational methods for solving the full potential equation. The finite volume algorithm of Jameson and Caughey[1,2] improves the capability to handle complex geometries, while the incorporation of the multigrid scheme[3,4] improves the computational efficiency. However, difficulty still exists in developing a general and reliable grid-generation scheme for realistic wing-body combinations. For example, FLO-28,[1] despite its reliability, does not map the crown line, the intersection of fuselage and symmetry plane, to a coordinate line. This results in undesirable pressure oscillations calculated along the crown line. FLO-30,[2] despite its better representation of fuselage cross sections, introduces a singular line upstream of the fuselage nose, resulting in an unrealistic modeling of the fuselage nose. Both FLO-28 and FLO-30 apply a sequence of mapping and shear transformations to generate grid systems in the flowfield. This process is tedious because of the need to work with different aspects of mapping singularities and is generally restricted to simple wing-body combinations. More general numerical grid-generation schemes have been developed by mapping the crown line to a coordinate line with improved flow solutions obtained in the corresponding modified versions of FLO-28.[5,6]

The grid topologies used in FLO-28 and also in Refs. 5 and 6 consider the fuselage surface and the vertical symmetry plane being mapped to the same coordinate surface such that an existing wing-alone code can be modified easily to include the fuselage effect. This results in highly distorted meshes near the crown line, and also unnecessary clustering of mesh points in the far field. In this paper, an improved grid topology is introduced that is similar to the FLO-30 grid topology without the singular line. A hybrid mapping/numerical grid-generation scheme is developed, and the multigrid flow solver of FLO-30 is modified to compute the flowfield based on the new grid. A second-order scheme of Chen[7] is incorporated for calculating fully and partially conservative solutions. A nonconservative scheme, using a similar upwind differencing in supersonic regions as in FLO-22,[8] is also included. Solutions have been obtained for a wide range of wing-body configurations. Typical solutions are presented and discussed.

Presented as Paper 84-2157 at the AIAA Second Applied Aerodynamics Conference, Seattle, WA, Aug. 21-23, 1984; received Oct. 8, 1984; revision received Feb. 22, 1985. Copyright © American Institute of Aeronautics and Astronautics, Inc., 1985. All rights reserved.

*Senior Staff Engineer, Research and Technology, Aircraft Configuration and Performance. Member AIAA.

†Engineer/Scientist—Specialist, Research and Technology, Aircraft Configuration and Performance. Member AIAA.

‡Senior Engineer/Scientist, Research and Technology, Aircraft Configuration and Performance. Member AIAA.

Modeling of Wing-Fuselage Geometries

In the application of the present finite difference scheme, the geometries of the wing and fuselage surfaces are represented by a fixed number of grid points on boundary planes. In order to model the wing-fuselage geometries accurately, the fuselage contours and the wing cross sections are first input and expressed in algebraic form; then, through a proper discretization, the grid points are distributed on the wing and fuselage surfaces.

To define a wing geometry, a number of airfoil sections at different span locations are required. These airfoil sections are interpolated to a fixed chordwise distribution to ensure that corresponding points at each span station are at the same x/c location. This wing definition is linearly interpolated to define the streamwise cuts at span stations specified by the grid-generation code.

The fuselage surface is input at several longitudinal stations as cross sections that are defined in the physical (x,y,z) coordinate system. These cross sections are then transformed to the polar coordinates (r,θ) with the origin at their centroids. Each (r,θ) cross-section definition is then represented by an analytical function, $r(\theta)$, through a Fourier series transformation. The Fourier series is then used to unwrap the fuselage surface about an arbitrary reference line to yield the curvilinear coordinates (x,d). A numerical iterative scheme was developed to determine the intersection point of a constant percent chord line on the wing with the fuselage cross-sectional contour. Using this procedure, a precise wing-fuselage intersection line is computed accurately in the physical space.

The grid points on the fuselage surface are distributed through the application of the so-called "wind tunnel mapping" function to be briefly described later. The grid distributions on the wing surface along each streamwise cut are contoured in the spanwise direction according to the computed intersection line. This allows clustering of mesh points near the fuselage, which is sometimes necessary to compute pressures on the fuselage more accurately.

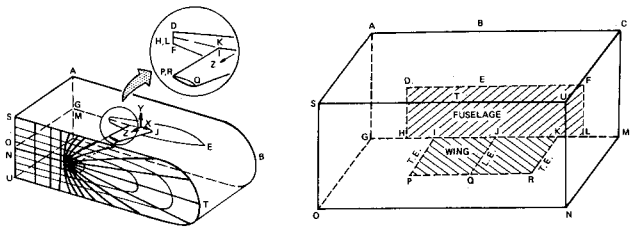

a) Physical. b) Computational.

Fig. 1 Physical and computational spaces of KGRID.

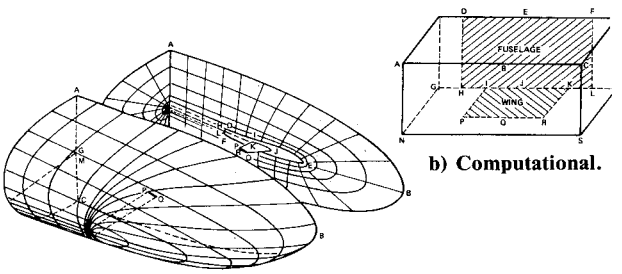

b) Computational.

a) Physical.

Fig. 2 Physical and computational spaces of PGRID.

Given the grid distributions computed on both the wing and fuselage surfaces, a hybrid mapping/numerical grid-generation scheme is then developed to distribute grid points in the flowfield. This will be described in the following section.

Grid-Generation Scheme

Two wing-body grid-generation codes, referred to as KGRID and PGRID, are considered, which use different grid topologies.

KGRID makes use of the same topology as FLO-28 and, therefore, can be used for the wing-alone case. Grid lines in all vertical planes parallel to the fuselage axis form C meshes, while grid lines in vertical planes perpendicular to the fuselage axis and in horizontal planes form H meshes. Grids are constructed by applying a transformation to map the fuselage onto the vertical symmetry plane (Fig. 1). PGRID makes use of a topology similar to FLO-30. This is different from the topology of FLO-28 and KGRID in that grid lines in planes perpendicular to the fuselage axis form O meshes and the fuselage and symmetry plane are mapped to two perpendicular coordinate surfaces in the computational space (Fig. 2). As a result, PGRID is more efficient in grid distribution than KGRID for the wing-body configurations. In KGRID, the spanwise far field is chosen to be a vertical plane, while in PGRID, the fuselage and the far-field boundary surfaces are described by two elliptic paraboloidal surfaces. Between these two boundary surfaces, a sequence of elliptic paraboloidal surfaces is generated. C-type meshes, generated by the so-called "wind tunnel mapping" function,[1,2] are distributed on each coordinate surface in both KGRID and PGRID.

A general elliptic paraboloid can be expressed as

$$\frac{y^2}{a^2(x)}+\frac{z^2}{b^2(x)}=\frac{x}{c(x)} \tag{1}$$

If a reference curve with $d=0$ is chosen to pass through the leading- and trailing-edge points of the wing cross section on the elliptic paraboloidal surface, a curvilinear coordinate system (x,d) on the surface can be obtained. The coefficients a, b, and c are chosen according to the grid distribution on the symmetry plane and wing planform. The (x,d) coordinates are transformed to (ξ,η) coordinates according to the following wind tunnel mapping function:

$$x+id=\ell n[1-\cosh(\xi+i\eta)] \tag{2}$$

where (x,d) coordinates are scaled such that the singular point, located half the leading-edge radius inside the leading-edge contour, is at $(\ell n 2,0)$. A mesh constructed by nearly constant ξ and η lines in the (ξ,η) plane is transformed to a C mesh on an elliptic paraboloid in the physical space.

The application of the mapping function maintains the orthogonality of the grid system in the mapped plane, but generally not in the other two cross planes, especially for cases where fuselage cross sections cannot be approximated by an ellipse. To improve the grid distribution near the fuselage surface in the fuselage cross plane, a numerical grid-generation scheme was developed. A system of elliptic equations can be formulated, as suggested in Ref. 6, based on the Cauchy-Riemann condition in the physical domain which satisfies the orthogonality condition. If ζ and η are assumed to be the real and imaginary parts of an analytical function $\theta=\zeta+i\eta$ of the complex variable $\sigma=s+it$, where s and t are curvilinear coordinates on the coordinate surface, then the Cauchy-Riemann conditions can be differentiated to yield

$$s_{\zeta\zeta}+s_{\eta\eta}=0 \tag{3}$$

$$t_{\zeta\zeta}+t_{\eta\eta}=0 \tag{4}$$

Frequently, it is desirable to introduce stretching functions so that mesh lines can be concentrated in regions of expected high gradients. In order to maintain orthogonality, stretching in the two directions must be uncoupled, that is,

$$Z=f(\zeta) \tag{5}$$

$$Y=g(\eta) \tag{6}$$

where Z and Y are the coordinates in the computational plane.

If both linear and quadratic stretching are considered in Eqs. (5) and (6), the elliptic equations (3) and (4) can be rewritten as[6]

$$C_1 s_{ZZ}+C_2 s_{YY}+C_3 s_Z+C_4 s_Y=0 \tag{7}$$

$$C_1 t_{ZZ}+C_2 t_{YY}+C_3 t_Z+C_4 t_Y=0 \tag{8}$$

where

$$C_1=1/\zeta_Z^2 \tag{9}$$

$$C_2=1/\eta_Y^2 \tag{10}$$

$$C_3=-\zeta_{ZZ}/\zeta_Z^3 \tag{11}$$

$$C_4=-\eta_{YY}/\eta_Y^3 \tag{12}$$

The coefficients C_1 and C_2 account for the linear stretching. By applying the Cauchy-Riemann condition, the ratio of C_1 to C_2 can be expressed as

$$C_1/C_2=\eta_Y^2/\zeta_Z^2=(s_Y^2+t_Y^2)/(s_Z^2+t_Z^2) \tag{13}$$

The coefficients C_3 and C_4 account for the quadratic stretching. These coefficients were computed explicitly in Ref. 6 and were found to be important in maintaining the mesh orthogonality in a highly stretched grid. A more thorough study reveals that these coefficients can be computed implicitly during a stable iteration scheme by using the following relations:

$$C_3=-\frac{1}{2}\left[\frac{\partial}{\partial Z}(s_Z^2+t_Z^2)\right]\frac{(s_Y^2+t_Y^2)}{(s_Z^2+t_Z^2)} \tag{14}$$

$$C_4=-\frac{1}{2}\left[\frac{\partial}{\partial Y}(s_Y^2+t_Y^2)\right]\frac{(s_Y^2+t_Y^2)}{(s_Z^2+t_Z^2)} \tag{15}$$

In the physical space, curvilinear coordinates (s,t) can be linearly transformed to Cartesian coordinates (x,y,z); therefore, Eqs. (7) and (8) can be rewritten as

$$C_1 x_{ZZ} + C_2 x_{YY} + C_3 x_Z + C_4 x_Y = P(Z,Y) \tag{16}$$

$$C_1 y_{ZZ} + C_2 y_{YY} + C_3 y_Z + C_4 y_Y = Q(Z,Y) \tag{17}$$

$$C_1 z_{ZZ} + C_2 z_{YY} + C_3 z_Z + C_4 z_Y = R(Z,Y) \tag{18}$$

where

$$C_1 = x_Y^2 + y_Y^2 + z_Y^2 \tag{19}$$

$$C_2 = x_Z^2 + y_Z^2 + z_Z^2 \tag{20}$$

$$C_3 = -\frac{1}{2}\left[\frac{\partial}{\partial Z}(x_Z^2 + y_Z^2 + z_Z^2)\right]\frac{(x_Y^2 + y_Y^2 + z_Y^2)}{(x_Z^2 + y_Z^2 + z_Z^2)} \tag{21}$$

$$C_4 = -\frac{1}{2}\left[\frac{\partial}{\partial Y}(x_Y^2 + y_Y^2 + z_Y^2)\right]\frac{(x_Z^2 + y_Z^2 + z_Z^2)}{(x_Y^2 + y_Y^2 + z_Y^2)} \tag{22}$$

The source terms P, Q, and R are added to the right-hand side of the equations because a certain degree of local mesh nonorthogonality may be unavoidably introduced when prescribing boundary points. The source terms can be computed explicitly along the boundaries and can be distributed into field points such that nonorthogonal grids along the boundary can change smoothly to orthogonal grids away from the boundaries. A line relaxation scheme was developed to solve the preceding equations with adequately prescribed boundaries.

It should be pointed out that the system of equations described in Eqs. (16-18) is different from Thompson's equations,[9] which are derived from another Cauchy-Riemann condition in the transformed domain. It can be shown that the original Thompson's equations can also satisfy the orthogonality condition in the physical space if the grid stretching is linear. However, if the grid stretching is nonlinear, Thompson's equations do not satisfy the orthogonality condition and, therefore, require various forms of source terms to control mesh sizes and orthogonality in various regions. The determination of these source terms is generally region-dependent; therefore, the mesh control is accomplished locally. In the present method global mesh control can be made by carefully prescribing nearly conformal boundaries and solving the equations that satisfy an approximate orthogonality condition. The grid system thus obtained is nearly orthogonal, at least in two planes, i.e., the mapping and fuselage cross planes, while the orthogonality of the grid system in the third cross plane can be well maintained by smoothly varying the coefficients defining the elliptic paraboloidal surfaces.

The hybrid mapping/numerical grid-generation method thus developed for KGRID and PGRID retains the simplicity and orthogonality of a mapping-generated grid in the far field, and also maintains the generality of a numerically generated grid in the near field. The mapping procedure is economical in generating grids away from the surfaces, and generally provides nearly conformal grids along the boundaries before the application of the numerical grid-generation procedure. Because the numerical procedure is applied only in the near field, the total computing cost is only a fraction of what it would be if it were applied everywhere. However, the main advantage of the present method is its ability to maintain the grid orthogonality almost everywhere in the flowfield. Precise mesh control can be exercised in the far field by applying the mapping procedure, while almost equally precise mesh control can also be exercised in the near field by solving the nearly conformal elliptic equation numerically.

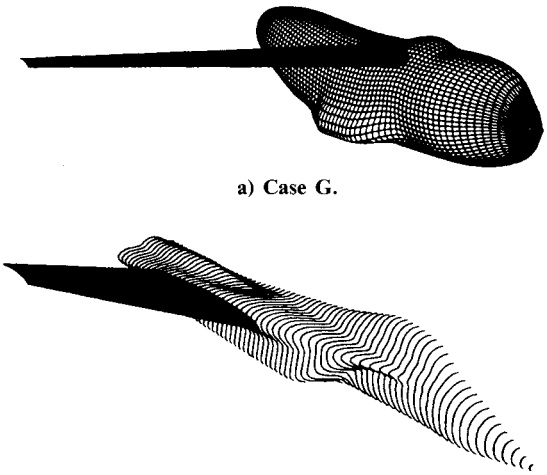

a) Case G.

b) Fighter.

Fig. 3 Input geometries.

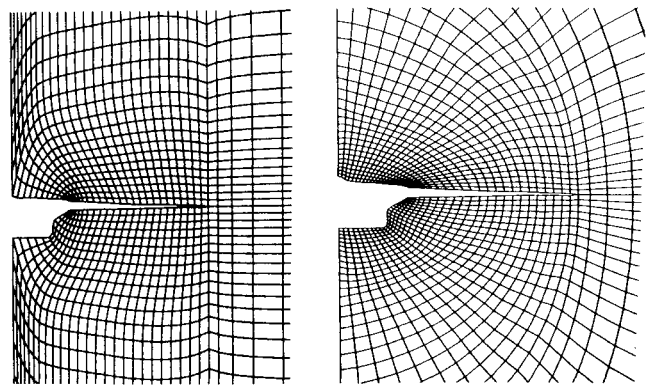

a) KGRID. b) PGRID.

Fig. 4 Grid distributions obtained by KGRID and PGRID on a typical fighter fuselage cross section.

Typical results obtained from KGRID and PGRID are presented in Figs. 3-6. The input geometries for a typical high-wing, wide-body military transport configuration, designated case G, and a typical fighter wing-body configuration are shown in Fig. 3. Case G has a landing gear pod underneath the wing, while the typical fighter configuration has a complex inlet entrance face that is currently modeled as a no-flux solid surface. Both the gear pod in case G and the inlet in the typical fighter configuration represent geometric complexities that are difficult to model in other wing-body codes. In Fig. 4 the grid distribution obtained by KGRID and PGRID on a fuselage cross section for the fighter configuration is presented. By solving Eqs. (16-18) iteratively with proper source terms included, grid lines are conformed to the boundary surfaces and intersect the boundaries at acceptable angles. In both the KGRID and PGRID solutions, a total of $160\times24\times32$ mesh cells is used. However, because of improved grid distribution, the total number of grid points on the fuselage surface in PGRID is twice that in KGRID, resulting in a better fuselage definition, or for the same number of wing/fuselage surface grid points, the total number of grid points in the flowfield can be reduced by 50% in PGRID. In addition, KGRID exhibits undesirable mesh distortion near the crown line corner as shown in Fig. 4a. Figure 5, showing horizontal views of case G, illustrates the superiority of PGRID over KGRID and FLO-30 in distributing points near the fuselage nose. The clustering of grid points near the fuselage nose is essential to resolve local high-pressure gradients. Figure 6 shows oblique views of the A-7 and emphasizes the singular line that must

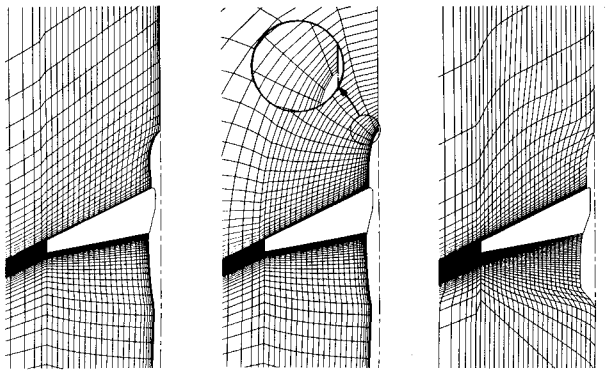

Fig. 5 Grid distributions obtained by KGRID, PGRID, and FLO-30 on a horizontal plane.

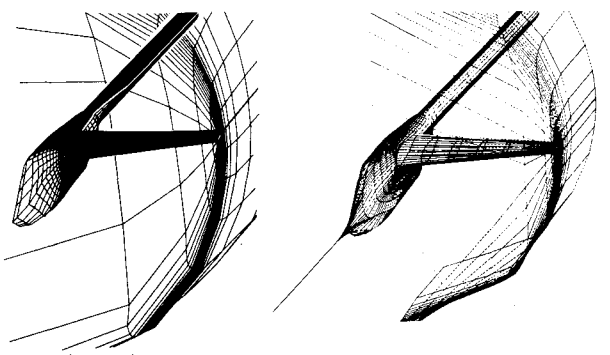

a) PGRID. b) FLO-30.

Fig. 6 Comparison of grid distributions on A-7 wing-fuselage surface obtained by PGRID and FLO-30.

be present in FLO-30, but not in PGRID. The cylindrical transformation used in generating the FLO-30 grid is singular along a line upstream of the fuselage nose. The singularity merges several coordinate lines to a straight line running from the fuselage nose to upstream infinity, thus creating an artificial sting with a highly distorted mesh in its neighborhood. Furthermore, the FLO-30 grid has a poorer fuselage geometry definition in the nose area because only about two-thirds of the C-mesh lines are used to define the surface geometry, while the other one-third is wasted in defining the artificial sting.

Potential Flow Solver

A multigrid transonic potential flow solver, FLO-27MPG, was developed by modifying the wing-alone code FLO-27M for the incorporation of KGRID. The topology of KGRID is similar to that of FLO-27M in the computational space. This allows the extension of the wing-alone code to handle a wing-body configuration simply by replacing the wing-alone grid with a wing-body grid. This can be done without modifying the flow equation solver. Therefore, it also retains the capability to compute wing-alone solutions. Another multigrid transonic potential flow solver, DFLO-30, was developed by modifying FLO-30M, a multigrid version of FLO-30, for the incorporation of PGRID. In FLO-30, no valid flow equation can be applied along the singular line upstream of the fuselage nose because of the singularity of the Jacobian transformation, therefore, the reduced potential function is explicitly set to zero along this singular line. This condition is equivalent to a nearly freestream condition, and thus not appropriate, especially near the fuselage nose where significant pressure gradients exist, and therefore restricts the application of FLO-30 to certain wing-body combinations where the fuselage nose effect is not pronounced. The singular line is not present in PGRID. Therefore, this difficulty does not appear in DFLO-30.

The basic finite volume formulation has been introduced in Refs. 1 and 2, while the multigrid scheme used in both FLO-27M and 30M has been described in Refs. 3 and 4. A first- and second-order, fully conservative and partially conservative scheme of Chen[7] was incorporated into DFLO-30. The partially conservative solutions are obtained by adjusting an artificial mass flux added at the shock points. Details of the scheme can be found in Ref. 7 and will not be duplicated here. However, an alternative form of artificial viscosity is considered here for a possible simulation of nonconservative solutions that have been obtained by using existing nonconservative schemes, such as in FLO-22. To introduce such an artificial viscosity, the second derivatives of the potential function ϕ in the streamwise direction, s, can be expressed in the computational space as

$$\phi_{ss} = (1/q^2)(U^2\phi_{XX} + V^2\phi_{YY} + W^2\phi_{ZZ} + 2UV\phi_{XY} + 2VW\phi_{YZ} + 2UW\phi_{XZ}) \tag{23}$$

where U, V, and W are contravariant components of velocity vectors, and q is the magnitude of the velocity.

If only the leading terms on the right-hand side of the above equations are considered, a first-order nonconservative artificial viscosity H can be introduced at point (i,j,k) by applying an upwind differencing to the $(a^2 - q^2)\phi_{ss}$ term in the governing equation at supersonic points as follows:

$$H = \mu_{i,j,k}[U^2(-\phi_{i+m,j,k} + 3\phi_{i,j,k} - 3\phi_{i-m,j,k} + \phi_{i-2m,j,k}) + V^2(-\phi_{i,j+n,k} + 3\phi_{i,j,k} - 3\phi_{i,j-n,k} + \phi_{i,j-2n,k})] \tag{24}$$

In the above equation, $\mu_{i,j,k}$ is the switching function defined as

$$\mu_{i,j,k} = \max[1 - (a^2/q^2), 0]_{i,j,k} \tag{25}$$

where a is the speed of sound and m and $n = \pm 1$, according to the local flow direction.

The artificial viscosities in both the spanwise and surface normal directions are currently being ignored. H is then added to the governing finite difference equation derived by applying the finite volume scheme.

A first-order partially conservative scheme[7] can be developed by applying the following artificial viscosity:

$$H = \left(\frac{\mu U^2\phi_{xx}}{D}\right)_{i,j,k} - \left(\frac{\mu U^2\phi_{xx}}{D}\right)_{i-m,j,k} \tag{26}$$

at supersonic points, and

$$H_s = -P_s\left(\frac{\mu U^2\phi_{xx}}{D}\right)_{i-m,j,k} \tag{27}$$

at shock points, the first subsonic points just downstream of the shock. A second-order partially conservative scheme[7] can be developed by applying the following artificial viscosity:

$$H = \left(\frac{\mu U^2\phi_{xx}}{D}\right)_{i-2m,j,k} - 2\left(\frac{\mu U^2\phi_{xx}}{D}\right)_{i-m,j,k} + \left(\frac{\mu U^2\phi_{xx}}{D}\right)_{i,j,k} \tag{28}$$

at supersonic points, and

$$H_s = P_s\left[\left(\frac{\mu U^2\phi_{xx}}{D}\right)_{i-2m,j,k} - \left(\frac{\mu U^2\phi_{xx}}{D}\right)_{i-m,j,k}\right] \tag{29}$$

at shock points. P_s in Eqs. (27) and (29) is the parameter controlling partially conservative differencing. If $P_s = 1$, $(\mu U^2\phi_{xx})/D$ is conserved along i lines, and the scheme is fully conservative. If $P_s < 1$, a numerical mass flux is introduced at the shocks, modifying the shock location and

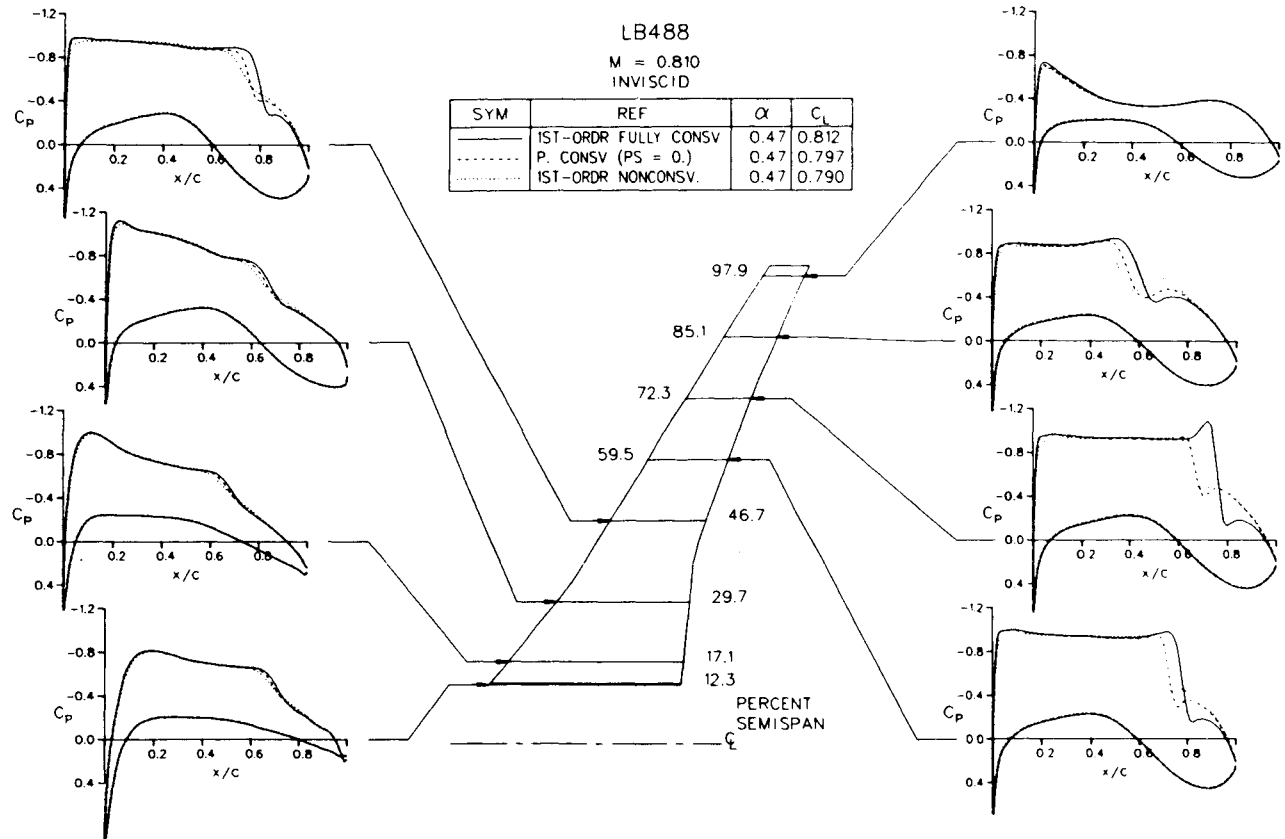

Fig. 7 Comparison of first-order fully conservative, partially conservative, and nonconservative solutions.

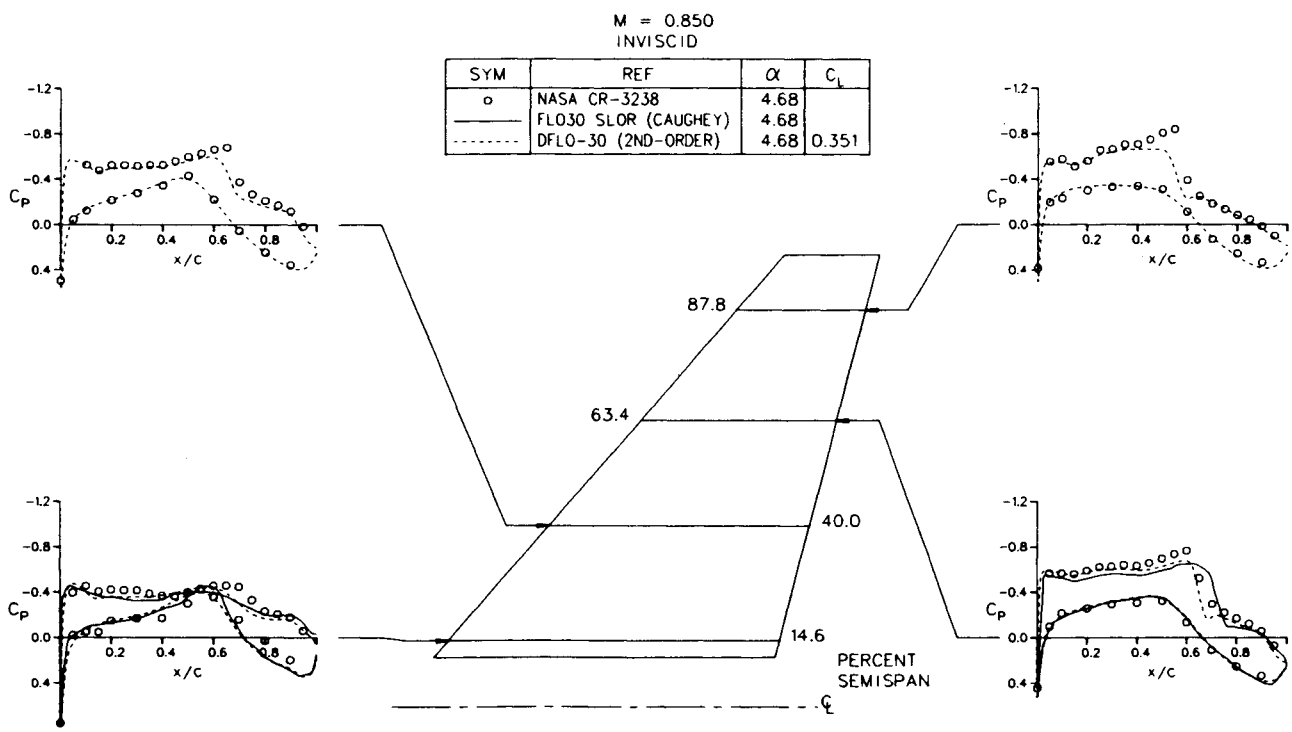

Fig. 8 Comparison of computed A-7 solutions with test data at $M_\infty = 0.85$ and $\alpha = 4.68$ deg.

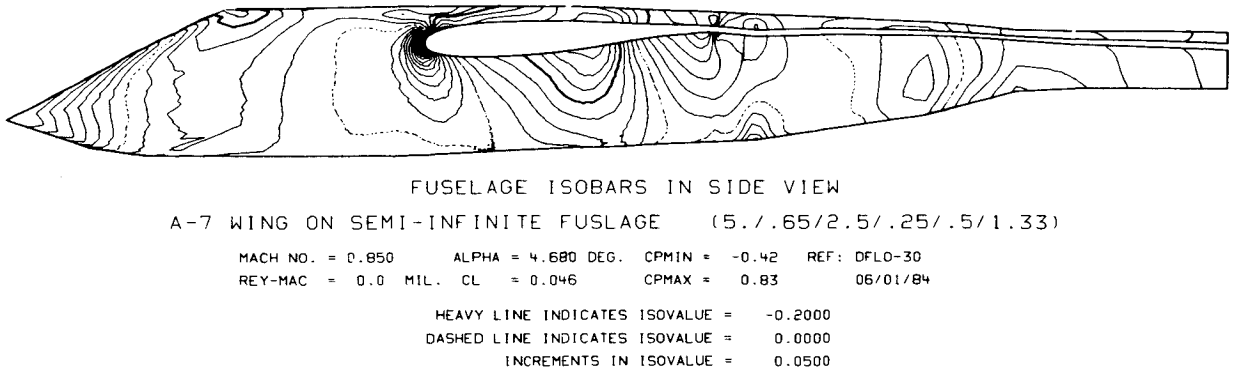

Fig. 9 Computed isobars on the A-7 fuselage surface.

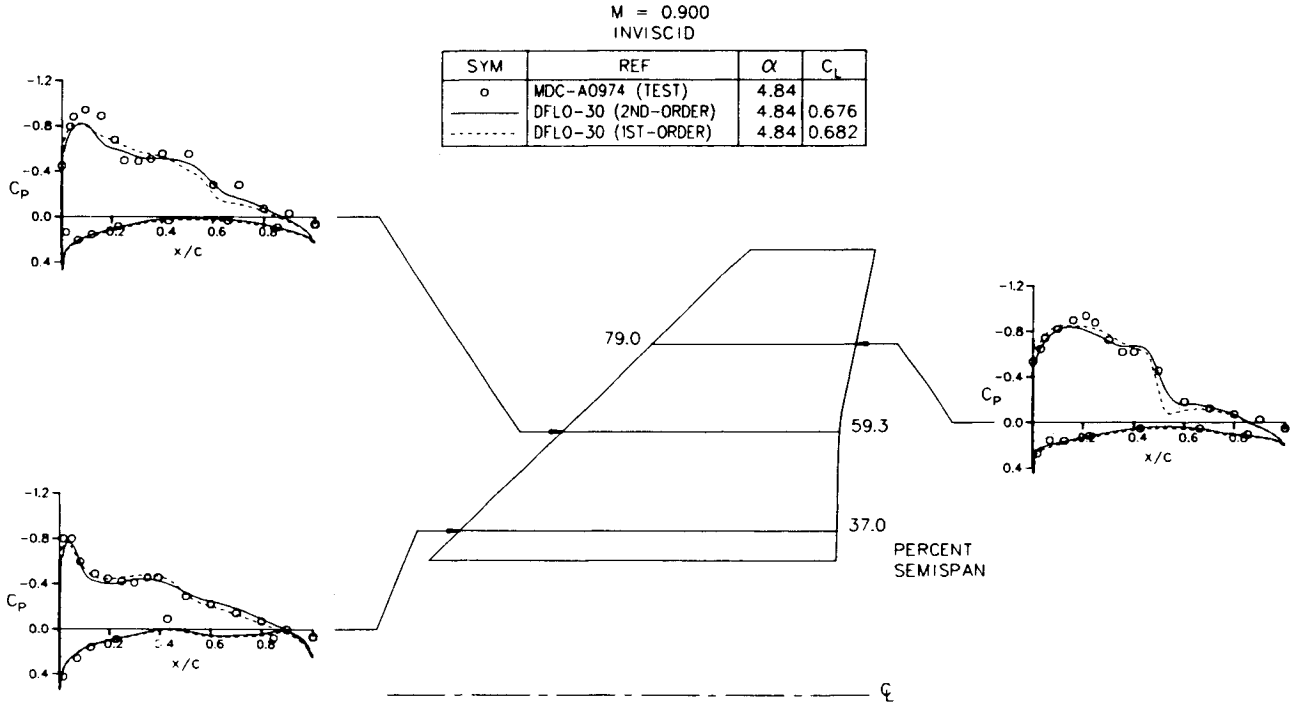

Fig. 10 Comparison of computed typical fighter configuration solutions with test data at $M_\infty = 0.900$ and $\alpha = 4.84$ deg.

strength. More detailed discussions of the partially conservative schemes have been given in Refs. 7 and 8. In an earlier study,[10] a two-dimensional channel flow calculation was made by applying both the first- and second-order partially conservative schemes, and the computed shocks in the channel were compared with the shock analytically obtained by the Rankine-Hugoniot relation. The study reveals that $P_s = 0.2$-0.3 generally produces shocks in good agreement with the Rankine-Hugoniot shocks. A similar conclusion was obtained by Lock.[11]

Numerical Results

Several wing-body configurations have been analyzed. These include the ONERA-M6, A-7, F-15, Douglas case G and wind tunnel models LB-435, LB-488, and LB-506. Some of them are extremely low-wing configurations such as LB-435 and LB-506, and some are extremely high-wing configurations, such as the F-15 and case G. Some have long and slender transport fuselage forebodies, such as LB-435, while some have sharp fuselage noses, such as the A-7 and F-15 configurations. Typical solutions obtained by using the PGRID/DFLO-30 code are presented in the following. More solutions can be found in Ref. 12. Unless stated otherwise, 160 mesh cells are used in the unwrapped wing cross-sectional direction, 16 cells in the wing surface normal direction, and 32 cells in the spanwise directions. Converged solutions are normally reached within 55 work units when the number of supersonic points computed in the flowfield ceases to change.

Comparisons of the fully conservative, partially conservative, and nonconservative solutions are presented in Fig. 7 for the LB-488 wing-body without viscous corrections. Solutions are obtained at $M_\infty = 0.81$ and $\alpha = 0.47$ deg. The fully conservative solution shows an undesirable preshock reexpansion near the 75% semispan location. This reexpansion tends to become more serious when the shocks become stronger. The partially conservative solution was obtained by setting $P_s = 0$. This is equivalent to adding numerical mass flux to account for the stagnation density change (or entropy change) across the shock and thus moving the shock upstream, and resulting in a weaker shock. The nonconservative solutions, obtained by applying Eq. (24), are very similar to the partially conservative solutions, except that the shock strength predicted in the nonconser-

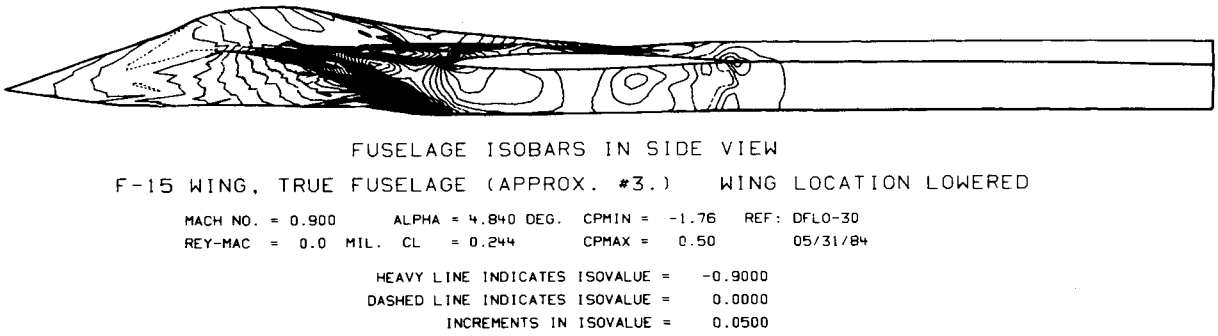

Fig. 11 Computed isobars on an F-15 fuselage surface.

	CODE	FIELD POINTS	REDUCTION/ WORK
—·—	FLO-22	192 x 24 x 32	0.9173
-------	FLO-27MPG	160 x 24 x 32	0.9261
—·—	DFLO-30	160 x 24 x 32	0.9033
——	DFLO-30	160 x 16 x 32	0.8955

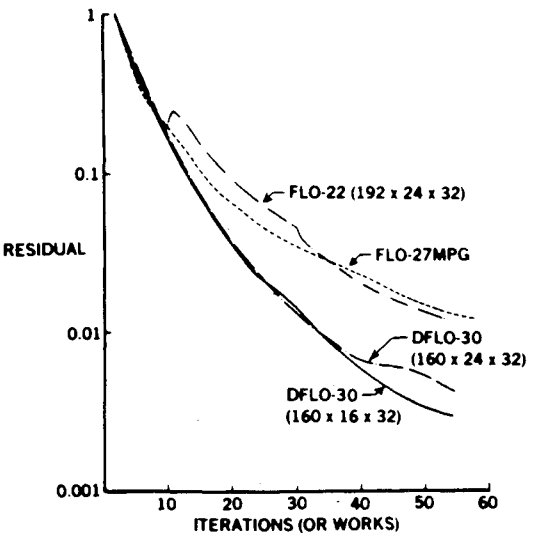

Fig. 12 Comparison of convergence histories of FLO-22, KGRID/FLO-27MPG, and PGRID/DFLO-30 solutions.

vative solution is slightly weaker, and after-shock re-expansion is generally smaller near the midspan. When coupled with a viscous flow calculation,[13] it was found that the nonconservative solutions generally agree better with test data than either fully or partially conservative solutions, especially in the prediction of shock strength and after-shock re-expansion.

A second-order partially conservative solution obtained with $P_s = 0.25$ for the A-7 wing-body is presented in Figs. 8 and 9 for $M_\infty = 0.851$ and $\alpha = 4.68$ deg. Figure 8 presents a comparison of the computed solution with test data.[14] Also shown is the FLO-30 solution obtained by a line relaxation scheme.[15] The present DFLO-30 solution agrees with test data better than the FLO-30 solution. Near the wing root, the FLO-30 solution overpredicts the lower surface pressure, probably due to inadequate modeling of the fuselage nose. At 63.4% semispan, the present solution predicts shock location better due to the use of the second-order partially conservative scheme. Figure 9 shows computed isobars on the A-7 fuselage surface for the same flow condition. Solutions obtained for the F-15, at $M_\infty = 0.900$ and $\alpha = 4.84$ deg are compared with test data[16] in Fig. 10. For a better geometry representation of the complex fuselage cross section, 24 mesh cells instead of 16 mesh cells are used in the wing surface normal direction. Both the first- and second-order partially conservative solutions are computed with $P_s = 0.25$. The second-order solution seems to resolve the experimentally observed double shock slightly better than the first-order solution. Figure 11 presents computed isobars on the F-15 fuselage surface. Evaluation of the quality of the grids is greatly aided by examining the isobar plots on the fuselage and wing surfaces. Because the side-mounted inlets on the F-15 fuselage were assumed to have no mass flux, and because their geometric representation was only approximate, the isobar solutions show slightly undesirable pressure peaks near the inlet leading edge. The solution is reasonable and well behaved elsewhere.

The convergence rates of typical FLO-22, KGRID/FLO-27MPG, and PGRID/DFLO-30 solutions are compared in Fig. 12 for the case of Fig. 7. The PGRID/DFLO-30 run converges better than either of the others. Since both DFLO-30 and FLO-27MPG apply the same multigrid scheme and the far-field locations in both solutions are about the same, the improvement of the convergence rate in DFLO-30 is probably due to the improved grid topology. The "reduction per work unit" shown in the figure is an average reduction of average residual per the equivalent computational effort of a fine-mesh iteration during the first 55 work units. In both FLO-27MPG and DFLO-30 runs, 14 multigrid cycles are used. Each multigrid cycle consists of three fine-mesh iterations, nine iterations each in the next two subgrid levels; and eight iterations in the coarsest subgrid level; therefore, one complete multigrid cycle is equivalent to 4.28125 work units. The value of reduction per work unit is 0.917 for the FLO-22, 0.926 for the FLO-27MPG, and 0.9035 and 0.8955 for the DFLO-30 solutions. Typical reduction per work unit for the same number of total work units shown in Ref. 4 for a typical FLO-30M solution is 0.92. The improvement of the convergence rate of DFLO-30 over that of FLO-30M could also be due to the improved mesh orthogonality near the fuselage nose.

Conclusion

A general and efficient transonic wing-body code, PGRID/DFLO-30, has been successfully developed. In FLO-22 and FLO-28 (or KGRID), unnecessary clustering of grid points occurs on the top and bottom far-field boundaries. The improved grid topology used in PGRID distributes usable grid points effectively between the near and far fields so that unnecessarily clustered grid points in the far field have been reduced significantly, resulting in a reduction of 30-50% of the grid points required in FLO-28 or 22 for a solution of equivalent accuracy. The convergence of solutions in DFLO-30 has been accelerated due to improved grid orthogonality. The overall improvement of the computational efficiency has made a PGRID/DFLO-30 wing-body run about 30% cheaper than a typical FLO-22 wing-alone run, while a typical KGRID/FLO-27MPG remains about 30% more costly than a typical FLO-22 run. Improved shock calculations have been obtained by introducing partially conservative and nonconservative artificial viscosities into a finite volume method.

Acknowledgment

This research was conducted under the Independent Research and Development Program of the McDonnell Douglas Corporation.

References

[1]Jameson, A. and Caughey, D. A., "A Finite Volume Method for Transonic Potential Flow Calculation," *Proceedings of AIAA 3rd Computational Fluid Dynamics Conference*, Albuquerque, NM, June 1977, pp. 35-54.

[2]Caughey, D. A. and Jameson, A., "Numerical Calculation of Transonic Potential Flow About Wing-Body Combinations," *AIAA Journal*, Vol. 17, Feb. 1979, pp. 175-181.

[3]Shmilovich, A. and Caughey, D. A., "Application of the Multi-Grid Method to Calculations of Transonic Potential Flow About Wing-Fuselage Combinations," NASA SP-2202, Oct. 1981, pp. 101-130.

[4]Caughey, D. A., "Multi-Grid Calculation of Three-Dimensional Transonic Potential Flows," AIAA Paper 83-0374, Jan. 1983.

[5]Yu, J. J., "Grid Generation and Transonic Flow Calculations for Three-Dimensional Configurations," AIAA Paper 80-1391, July 1980.

[6]Chen, L. T., Caughey, D. A., and Verhoff, A., "A Nearly Conformal Grid Generation Method for Transonic Wing-Body Flowfield Calculations," AIAA Paper 82-0108, Jan. 1982.

[7]Chen, L. T., "A More Accurate Transonic Computational Method for Wing-Body Configurations," *AIAA Journal*, Vol. 21, June 1983, pp. 848-855.

[8]Jameson, A. and Caughey, D. A., "Numerical Calculations of the Transonic Flow Past a Swept Wing," New York University, ERDA Rept. C00-3077-140, 1977.

[9]Thompson, J. F., Thames, F. C., and Mastin, C. M., "Automatic Numerical Generation of Body-Fitted Curvilinear Coordinate System for Field Containing any Number of Arbitrary Two-Dimensional Bodies," *Journal of Computational Physics*, Vol. 15, July 1974, pp. 299-319.

[10]Chen, L. T., "A Modified Shock-Point Operator with Stagnation-Density Correction," *Numerical and Physical Aspects of Aerodynamic Flows II*, edited by T. Cebeci, Springer-Verlag, New York, 1984, pp. 351-365.

[11]Lock, R. C., "A Modification to the Method of Garabedian and Korn," *Notes on Numerical Fluid Mechanics, Numerical Methods for the Computation of Inviscid Transonic Flows with Shock Waves*, Vol. 3, edited by A. Rizzi and H. Viviand, Friedrich Viewag & Sohn, Braunschweig/Wiesbaden, FRG, 1979.

[12]Chen, L. T., Vassberg, J. C., and Peavey, C. C., "A Transonic Wing-Body Flowfield Calculation with Improved Grid Topology and Shock-Point Operators," AIAA Paper 94-2157, Aug. 1984.

[13]Cebeci. T., Chen, L. T., Chang, K. C., and Peavey, C. C., "An Interactive Scheme for Three-Dimensional Transonic Flows," *Proceedings of the 3rd Symposium on Numerical and Physical Aspects of Aerodynamic Flows*, Long Beach, CA, Jan. 1984.

[14]Haney, H. P. and Johnson, R. R., "Application of Numerical Optimization to the Design of Wings with Specified Pressure Distributions," NASA CR 3238, Feb. 1980.

[15]Caughey, D. A. and Jameson, A., "Progress in Finite-Volume Calculations for Wing-Fuselage Combinations," *AIAA Journal*, Vol. 18, Nov. 1980, pp. 1281-1288.

[16]Verhoff, A. and O'Neil, P. G., "Extension of FLO Codes to Transonic Flow Prediction for Fighter Configurations," *Progress in Astronautics and Aeronautics: Transonic Aerodynamics*, edited by D. Nixon, Vol. 81, AIAA, New York, 1981, pp. 467-488.

From the AIAA Progress in Astronautics and Aeronautics Series...

LIQUID-METAL FLOWS AND MAGNETOHYDRODYNAMICS—v.84

Edited by H. Branover, Ben-Gurion University of the Negev
P.S. Lykoudis, Purdue University
A. Yakhot, Ben-Gurion University of the Negev

Liquid-metal flows influenced by external magnetic fields manifest some very unusual phenomena, highly interesting scientifically to those usually concerned with conventional fluid mechanics. As examples, such magnetohydrodynamic flows may exhibit M-shaped velocity profiles in uniform straight ducts, strongly anisotropic and almost two-dimensional turbulence, many-fold amplified or many-fold reduced wall friction, depending on the direction of the magnetic field, and unusual heat-transfer properties, among other peculiarities. These phenomena must be considered by the fluid mechanicist concerned with the application of liquid-metal flows in partical systems. Among such applications are the generation of electric power in MHD systems, the electromagnetic control of liquid-metal cooling systems, and the control of liquid metals during the production of the metal castings. The unfortunate dearth of textbook literature in this rapidly developing field of fluid dynamics and its applications makes this collection of original papers, drawn from a worldwide community of scientists and engineers, especially useful.

Published in 1983, 454 pp., 6×9, illus., $25.00 Mem., $55.00 List

TO ORDER WRITE: Publications Order Dept., AIAA, 1633 Broadway, New York, N.Y. 10019